Tellus (2003), 55A, 31–44
Printed in UK. All rights reserved

TELLUS
ISSN 0280–6495

The effects of closure-based eddy diffusion on the climate and spectra of a GCM

By JORGEN S. FREDERIKSEN*, MARTIN R. DIX and ANTONY G. DAVIES, *CSIRO Atmospheric Research, PMB1, Aspendale, Victoria 3195, Australia*

(Manuscript received 27 June 2001; in final form 2 April 2002)

ABSTRACT

A recently developed horizontal eddy diffusion parameterization based on closure theory has been implemented in the CSIRO atmospheric global climate model (GCM). Detailed studies of the effects of the parameterization on the simulated atmospheric circulation, transient kinetic energy and kinetic energy spectra have been carried out for different months throughout the year. These diagnostics have been compared with corresponding results from observations and from control simulations using an ad hoc diffusion parameterization also employed in earlier works with this model. The new diffusion parameterization has improved the simulated atmospheric circulation in the following ways. Zonal and total wavenumber spectra now have approximate -3 power laws for ranges of intermediate wavenumbers, as in the observations, while the control simulation spectra are considerably flatter. Peak values of transient kinetic energy near the tropospheric jet cores are considerably larger than in the control and in better agreement with observations, particularly in boreal winter. The strength and location of the tropospheric jets are also improved with the new diffusion parameterization, with monthly averaged zonal mean winds in the Northern Hemisphere and Southern Hemisphere jet cores stronger than for the control by as much as 5 m s^{-1} in boreal winter and spring. The GCM simulations are also stable with longer timesteps with the new eddy diffusion parameterization. It is suggested that further improvements in GCM simulations may be achievable through parameterizations of the nondiagonal elements of the covariance matrix of eddy fluxes such as the eddy-topographic force.

1. Introduction

The accuracy of climate simulations, and predictions of weather and climate, by global climate models (GCMs) is strongly dependent on the appropriate treatment of subgrid scale processes, which cannot be explicitly resolved at the finite resolutions of the GCMs. A long-standing problem of GCMs has been the significant errors in their simulations of kinetic energy and in its partitioning between eddy kinetic energy and zonal mean kinetic energy. Typically, GCMs lose transient eddy kinetic energy and gain zonal kinetic energy when integrated from observed initial conditions. This was a problem with the earliest models of Smagorinsky et al. (1965), Manabe et al. (1965, 1970, 1979), Miyakoda et al. (1971) and Baer and Alyea (1971). The early literature is further reviewed by Frederiksen and Sawford (1980). To some extent it has also been a problem with more recent models as discussed for example by Hollingsworth et al. (1987) and Frederiksen et al. (1996). The sensitivity of the large-scale kinetic energy to resolution and to the strength of the diffusion parameterization, as found by Manabe et al. (1979), was also replicated by Laursen and Eliasen (1989) and Eliasen and Laursen (1990), who used higher order diffusion operators to account for the dissipative effects of the unresolved scales.

Frederiksen et al. (1996) argued that the parameterization and strength of the eddy dissipation play major roles in the shape of kinetic energy spectra and in the partitioning of kinetic energy between eddy kinetic energy and zonal mean kinetic energy. They examined

*Corresponding author.
e-mail: jorgen.fredriksen@csiro.au

the resolution dependence of kinetic energy spectra and provided a dynamical explanation for the so-called 'tail wagging the dog' effect whereby scale-selective dissipation operators cause a drop in the tail of the energy spectra and, surprisingly, also an increase in the large-scale energy. They showed that the cause of this effect relied on the fact that the dissipation operators dissipate enstrophy while leaving the total kinetic energy approximately conserved. A canonical equilibrium model of the effect was presented, and it was argued that more soundly based eddy viscosity parameterizations were needed to maintain the correct kinetic energy spectra with changing resolution and to maintain the correct large-scale flow fields.

For the case of two-dimensional turbulence in planar geometry, Leith (1971) calculated a dissipation function that would maintain, as a statistically stationary state, a truncated –3 power law spectrum. He based his formulation on the eddy damped quasi-normal Markovian (EDQNM) closure (Leith, 1971). Frederiksen and Davies (1997; hereafter FD) developed eddy drain viscosity, stochastic backscatter and net eddy viscosity parameterizations in spherical geometry for two-dimensional turbulence based on EDQNM and direct interaction approximation (DIA) closure models (FD). They noted that subgrid scale eddies not only drain energy and enstrophy from the retained scale flow but also randomly force the retained scales. This injection of energy and enstrophy by the stochastic backscatter term contributes to the growth of instabilities which may otherwise be suppressed (Leith, 1990). FD showed that their parameterizations were able to maintain essentially the same large scale kinetic energy spectra with varying horizontal resolution in barotropic model simulations. They noted the much larger differences between spectra at different resolutions when using a number of different ad hoc eddy viscosity parameterizations. FD combined the effects of the eddy drain viscosity and stochastic backscatter to define a net eddy viscosity similar to conventional eddy viscosities. They found that the net eddy viscosity formulation is equally successful when the model contains reasonable amplitude random forcing or if the resolved scale flow is suitably chaotic. They also calculated Leith's (1971) dissipation function in spherical geometry for an n^{-3} kinetic energy spectrum and found it has considerably larger negative values at intermediate wavenumbers than FD's conventional net eddy dissipation (Fig. 14 of FD).

Parallel with these theoretical developments, empirical interaction functions (EIFs), representing net eddy dissipation, have been calculated from energy balance equations and based on observational or model data sets. Koshyk and Boer (1995) used ECMWF analyses to calculate the net eddy dissipation for vorticity as a function of total wavenumber n and vertical level at triangular T32 resolution. Subsequent model simulations incorporating their vorticity EIFs for all prognostic variables produced kinetic energy spectra in reasonably good agreement with observations but with somewhat too large amplitudes at the largest wavenumbers. Kaas et al. (1999) computed separate EIFs for vorticity, divergence and temperature for two different GCMs based on comparisons of model simulations at different resolutions. They found that the improvements in model simulations using empirically determined dissipation functions were model- and resolution-dependent, being generally more satisfactory at resolutions significantly higher than T21.

The purpose of this article is to examine the effects on the mean climate and transient eddy statistics and spectra of employing the FD net eddy diffusion parameterization in the CSIRO Mark 2 GCM. The above-mentioned previous studies have been for boreal winter flows. Here we have analysed the effects of the FD net eddy dissipation on the spectra and flows for different months throughout the year but again focussing on January. We also compare the GCM results with the FD net eddy diffusion with control simulations incorporating a Laplacian dissipation operator restricted to the largest wavenumbers, as also employed in earlier studies with the model. The CSIRO Mark 2 GCM, described in McGregor et al. (1993), has been extensively used for climate and climate change simulations (e.g. Dix and Hunt, 1995; Watterson et al., 1995, 1997; Gordon and O'Farrell, 1997; Smith et al., 1997). More recent studies using a triangular T63 resolution, as employed in our current examination, include the works of Smith et al. (1998) and Smith (1999).

In Section 2 we summarize the formulation of the FD net eddy viscosity parameterization based on EDQNM and DIA closure models. Here we also define a normalized net eddy dissipation function whose functional form will be used in the subsequent sections to define the eddy diffusion. The CSIRO Mark 2 GCM is briefly described in Section 3, including the standard or control formulation of the horizontal diffusion parameterization. In this section we also examine the simulation of kinetic energy spectra and latitude-pressure cross sections of transient kinetic energy and of monthly averaged and zonally averaged zonal winds for each month of the year. These

simulations are compared with corresponding results based on ECMWF/TOGA basic level III data for the years 1985–1992 inclusive (ECMWF report, 1994).

In Section 4 we describe the incorporation of the FD net eddy viscosity parameterization in the CSIRO Mark 2 model and we compare the simulations with the corresponding results described in Section 3 for the control simulation. We examine the sensitivity of our simulations to the strength of the eddy diffusion. Our aim is to focus on the effects of parameterizations of unresolved horizontal scale interactions rather than to attempt to optimally tune the GCM by also altering other processes, such as for example gravity-wave drag parameterizations. Our conclusions are detailed in Section 5.

2. Closure-based eddy viscosity

FD developed self-consistent closure-based eddy viscosity and stochastic backscatter parameterizations in spherical geometry using EDQNM and DIA closures. In particular, they presented results pertaining to the monthly averaged observed spectrum for January 1979. They showed that the effects of the subgrid scale eddies consist of a drain of energy and enstrophy from the resolved scales, but that there is also an injection of energy and enstrophy to the resolved scales which is represented by a stochastic backscatter term. This injection may contribute to the growth of instabilities, which may be suppressed in lower-resolution simulations unless a stochastic backscatter term is included (Leith, 1990; Piomelli et al., 1991). However, most atmospheric circulation models have not accounted for the stochastic backscatter term, but have tried to account for the differences between the drain and injection terms through an effective viscosity.

FD define a (negative) eddy backscatter viscosity ν_b from the stochastic backscatter term [their Eq. (3.14)] and then define a net eddy viscosity ν_n as the sum of the eddy drain viscosity ν_d and the eddy backscatter viscosity ν_b [their Eq. (3.16)]. They show that such a representation of the subgrid scale eddies works very well when the barotropic model contains reasonable amplitude noise forcing (or if the resolved scale flow is suitably chaotic).

In this paper, we use net eddy viscosity parameterizations for which $\nu_n(n)n(n+1)$ is proportional to the normalized net eddy dissipation function $g(n/n_*)$, shown in Fig. 1, where n is the total 2D wavenumber

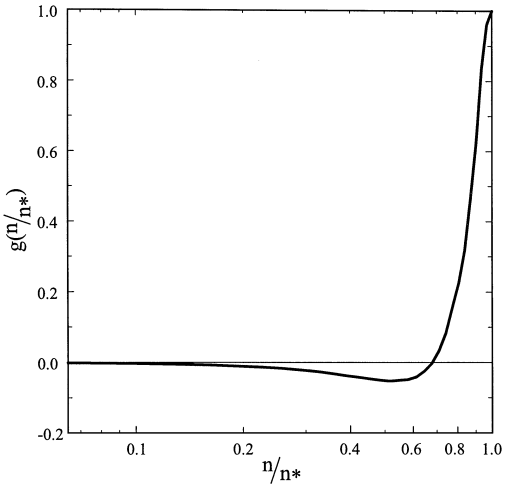

Fig. 1. Normalized net eddy dissipation function $g(n/n^*)$ as a function of normalized total wavenumber n/n^*.

and $n_* = T$ is the largest retained total wavenumber. The net eddy dissipation function has been obtained from the T31 simulations of FD (Fig. 3d of FD) in which the net eddy dissipation

$$\nu_n(n)n(n+1) = 0.067g(n/n_*), \tag{2.1}$$

$n_* = 31$ and $\nu_n(n)$ is nondimensional. The net eddy viscosity shown in Fig. 1 was calculated using EDQNM closure theory. Very similar results are obtained using DIA closure theory as shown in Fig. 9b of FD.

If the dissipation function (2.1) had been derived on the basis of spectra having an infinitely long n^{-3} enstrophy cascading inertial range then we would expect that it would satisfy a scaling relationship with varying resolution (Leith, 1971; FD). That is, the dissipation would have the universal form $g(n/n_*)$ for varying resolution n_*, but the strength of the dissipation required to maintain the n^{-3} inertial range as a statistically stationary state would depend on the resolution. Our spectra differ from this idealized form; in particular, they are more complicated at small wavenumbers and as a consequence we do not expect exact universality for our net dissipation function. However, we expect it to be approximately universal. Indeed, comparison of the net eddy viscosity of FD (Figs. 3c and 4) at T31 and T15 suggests such an approximate universality even at these rather low resolutions. This is also confirmed by a subsequent calculation of the net eddy dissipation at T63 (based on January 1979 vertically

integrated spectra reduced from T126 to T63 in barotropic simulations) that has essentially the same form as in Fig. 1 but with a relatively smaller negative contribution. In T63 barotropic simulations, the strength of the net eddy dissipation required to maintain the January 1979 spectrum is almost three times that at T31 [Eq. (2.1)].

3. GCM simulations with standard diffusion

The CSIRO atmospheric GCM that we use for the simulations described in this section and in Section 4 is described in detail by McGregor et al. (1993). Briefly the CSIRO Mark 2 model is a nine-level general circulation model that simulates the primitive equations of motion of the global atmosphere. It incorporates a comprehensive array of physical processes that force the dynamical and thermodynamic equations. It incorporates diurnal and seasonal cycles of forcing. It includes radiation and precipitation, and major properties such as snow, sea-ice and cloud amount are determined self-consistently. The model includes an interactive land-surface scheme, but sea-surface temperatures are prescribed in the version used for the present study and are interpolated in time from the monthly fields of the Bottomley et al. (1990) climatology for 1951–1980. Vertical diffusion in the model is parameterized in terms of a stability-dependent K theory following Blackadar (1962). The model uses the flux form of the dynamical equations.

The model uses the sigma coordinate in the vertical where $\sigma = p/p_s$ with p the pressure and p_s the surface pressure. The main prognostic variables are the surface pressure p_s, and the surface pressure weighted vorticity, $\hat{\zeta} = p_s\zeta$, divergence, $\hat{D} = p_s D$, temperature $\hat{T} = p_s T$ and moisture mixing ratio $\hat{q} = p_s q$ at all levels. These variables are carried as spherical harmonic coefficients or spectral fields except for the moisture mixing ratio, which is carried on a Gaussian grid. The current version of the model uses the sigma levels

(0.9793, 0.9136, 0.8032, 0.6598, 0.5000, 0.3401, 0.1968, 0.0864, 0.0208)

for calculation of the main prognostic variables. It also uses a horizontal resolution corresponding to triangular truncation T63. It uses a semi-implicit leap-frog time-stepping scheme together with an Asselin time filter. The timestep used in these simulations varies between 4 and 15 min.

3.1. Standard horizontal diffusion parameterization

Horizontal diffusion is applied to the surface pressure weighted vorticity $\hat{\zeta}$, divergence $\hat{D}$ and temperature fields $\hat{T}$. It is not applied to the surface pressure or to the moisture mixing ratio which is treated using a semi-Lagrangian advection scheme that is slightly diffusive (McGregor, 1993). Let $\hat{\zeta}_{mn}$, $\hat{D}_{mn}$ and $\hat{T}_{mn}$ represent the dimensional spectral coefficients of $\hat{\zeta}$, $\hat{D}$ and $\hat{T}$ respectively. Then the standard diffusion parameterizations for vorticity, divergence and temperature have the forms

$$\frac{\partial \hat{\zeta}_{mn}}{\partial t} \sim -\frac{K_\zeta^{\mathrm{d}}}{a^2}\Delta(n)n(n+1)\hat{\zeta}_{mn} \tag{3.1a}$$

$$\frac{\partial \hat{D}_{mn}}{\partial t} \sim -\frac{K_D^{\mathrm{d}}}{a^2}\Delta(n)n(n+1)\hat{D}_{mn} \tag{3.1b}$$

$$\frac{\partial \hat{T}_{mn}}{\partial t} \sim -\frac{K_T^{\mathrm{d}}}{a^2}\Delta(n)n(n+1) \times \left\{\hat{T}_{mn} - \left(\bar{T} + \sigma\frac{\partial \bar{T}}{\partial \sigma} - T_{\mathrm{o}}\right)p_{\mathrm{s}\,mn}\right\}. \tag{3.1c}$$

where $\sim$ denotes the usual nonlinear terms in addition to the explicit diffusion terms shown.

Here a is the earth's radius, $\bar{T}$ is the global mean σ-level temperature and T_{o} is an isothermal temperature taken as 290 K. The function $\Delta(n)$ is a cut-off function which restricts the dissipation to the small scales; the standard diffusion parameterization at T63 uses

$$\Delta(n) = \begin{cases} 1 & 60 \le n \le 63 \\ 0 & \text{otherwise} \end{cases} \tag{3.2}$$

resulting in a very scale-selective dissipation operator. The standard diffusion parameterization also uses the dimensional vorticity diffusion coefficient $K_\zeta^{\mathrm{d}} = 6.25 \times 10^4\ \mathrm{m^2\ s^{-1}}$ corresponding to a nondimensional coefficient of $K_\zeta = 2.112 \times 10^{-5}$ [where we use a (earth's radius) and Ω^{-1} (earth's angular velocity)$^{-1}$ as length scales and time scales]. It also sets $K_T^{\mathrm{d}} = K_\zeta^{\mathrm{d}}$ and $K_D^{\mathrm{d}} = 4K_\zeta^{\mathrm{d}}$; the larger diffusion coefficient for divergence was chosen to ensure numerical stability in the stratosphere for reasonably large time steps (Gordon, 1999; personal communication).

After an initial 50-yr spin up, in which the CSIRO GCM reached its climatological state, the model was further integrated in the control mode for 10 yr. This 10-yr data set was then used to generate the kinetic energy spectra, kinetic energy cross-sections and mean

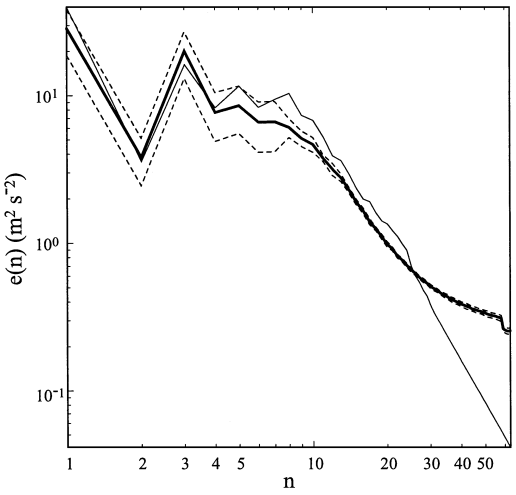

Fig. 2. Kinetic energy spectra $e(n)\,(\mathrm{m}^2\,\mathrm{s}^{-2})$ for January 1979 (thin solid), control GCM simulation for January (thick solid), $e(n) \pm \sigma(n)$ (dashed) for control simulation for January.

zonal wind cross-sections described in the following subsections.

3.2. Kinetic energy spectra for control simulation

Next, we examine the kinetic energy spectra for the control simulation focussing on the results for January for comparison with the observed spectra for January 1979. Figure 2 shows the mean and mean $\pm$ standard deviation of the dimensional total wavenumber kinetic energy spectrum $e(n)$ in $\mathrm{m}^2\,\mathrm{s}^{-2}$ for January for the control GCM simulation. Here the kinetic energy spectra include both the rotational and divergent components of the wind and are averages over the model levels and the 10 simulated Januaries. We see from Fig. 2 that the control simulation underestimates the kinetic energy at total wavenumbers between 5 and 25 compared with the observed spectra for January 1979. At small scales the kinetic energy is too large compared with the observations extrapolated as an $[n(n+1)]^{-3/2}$ spectrum matched to observations at $n = 31$. The January 1979 spectrum is very similar to that in Fig. 9 of Kaas et al. (1999) based on ECMWF reanalysis data for January (1982, 85, 88 and 91) data. The control zonal wavenumber spectrum $E(m)$ (not shown) is again flatter than observed (Wiin-Nielsen, 1967, 1972; Leith, 1971), being closer to an m^{-2} spectrum than to an m^{-3} spectrum between $m \sim 7$ to 40.

The less than optimal choice of the control horizontal diffusion employed in earlier works with the CSIRO GCM (Smith et al., 1998; Smith, 1999) provides an example of the 'tail wagging the dog' effect. From the modelling studies on the role of the strength of the diffusion on spectra and circulation reviewed in the Introduction, it is expected that the too flat control spectrum at small scales and the too low energy at intermediate scales is symptomatic of this effect. That is, the scale-selective dissipation is too weak, resulting in an increase of kinetic energy at small scales and, for the reasons outlined by Frederiksen et al. (1996), a decrease in kinetic energy at intermediate and some large scales. As noted by Frederiksen et al. (1996), the counter-intuitive behaviour at intermediate and large scales is due to the fact that scale-selective diffusion operators dissipate enstrophy but have less effect on the energy. Thus decreasing the scale-selective dissipation will tend to increase the enstrophy to energy ratio and result in a flat spectrum, while increasing the dissipation will decrease this ratio and send excess energy to larger scales and result in a steeper spectrum. We also notice from Fig. 2 that there is a distinct drop in the kinetic energy spectrum at wavenumbers 60–63. This is a reflection of the fact that the scale selection operator $\Delta(n)$ in Eq. (4.2) for the control run is too scale selective. It attempts to confine the dissipation range to the wavenumbers $n \sim 60$ to 63.

3.3. Transient kinetic energy cross sections

Many models of the atmospheric general circulation tend to have too little transient kinetic energy, as reviewed in the Introduction. This is also the case with the control CSIRO Mark 2 model as shown in Fig. 3. Figure 3a shows cross sections of zonally averaged transient kinetic energy based on twice daily January ECMWF/TOGA basic level III data for the years 1985–1992, while Fig. 3b shows the corresponding cross-sections for the control simulation based on twice daily data for January for 10 yr of integration. We note the significantly smaller peak amplitudes in both the Northern and Southern Hemispheres in the control simulation compared with the observations. For example, in the Northern Hemisphere the peak transient kinetic energy is 189 $\mathrm{m}^2\,\mathrm{s}^{-2}$ in the control compared with 220 $\mathrm{m}^2\,\mathrm{s}^{-2}$ at 300 hPa near 50°N and 231 $\mathrm{m}^2\,\mathrm{s}^{-2}$ at 250 hPa near 40°N in the observations, and in the Southern Hemisphere it is 144 $\mathrm{m}^2\,\mathrm{s}^{-2}$ in the control compared with 219 $\mathrm{m}^2\,\mathrm{s}^{-2}$ in the observations.

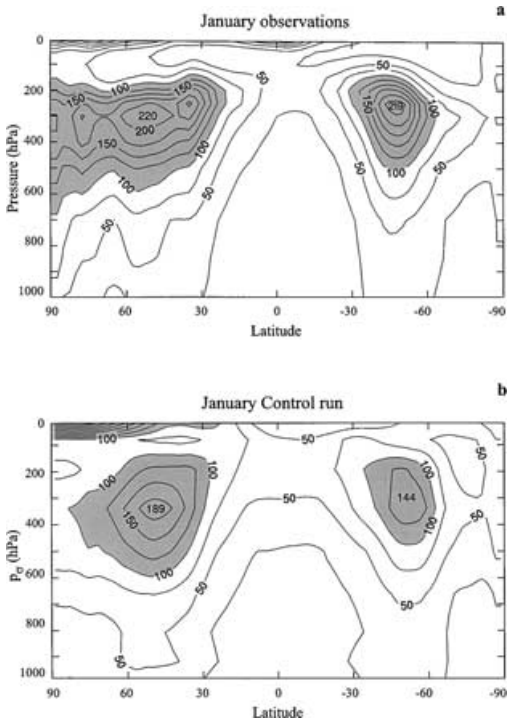

Fig. 3. (a) Monthly and zonally averaged transient kinetic energy cross-sections ($m^2\ s^{-2}$) as functions of latitude and pressure p for January ECMWF analyses for 1985 to 1992. Shading above 100 $m^2\ s^{-2}$. (b) As in (a) for control simulations as functions of latitude and $p_\sigma = 1000\sigma$.

The results in Fig. 3b have been obtained using a 4-min time-step in the simulations. Increasing the time-step above this to, say, 15 min which is commonly used with a T63 resolution, results in large-amplitude spurious transients throughout the atmosphere over the south polar latitudes. In Section 4 we note that these spurious transients result from inadequacies in the standard diffusion parameterization with the larger time-step.

3.4. Mean zonal winds

Next we compare the control zonal mean wind cross-sections based on 10 yr of simulation with ECMWF analyses for the period 1985–1992. These have been calculated for each month, but we shall focus here on the averages for January and April and to a lesser degree for October and July; we find that the impact of the FD parameterization is largest in boreal winter and spring, followed by autumn and is least in summer. Figure 4 shows the mean zonal winds for the observations and control simulations in January, April and October. For January we note that while the main features of the circulation are simulated, both the Northern and Southern Hemisphere jetstream maxima are underestimated and the Northern Hemisphere stratospheric jet is too weak. In these respects, the current T63 control simulation is similar to the rhomboidal R21 control simulation of McGregor et al. (1993, Fig. 8a) for December–January–February. Between January and April the strength of the Northern Hemisphere tropospheric jet decreases in the observations and, by a larger factor, in the control simulations. The resultant jetstream maximum in the control run in April is about 8 m s^{-1} weaker than in the observations. In both January and April, and in the intervening months, the Northern Hemisphere tropospheric jetstream maxima also tend to be displaced poleward in comparison with the observations. In general, comparison between observations and the control run tends to be better in the Southern Hemisphere during this period, although in the control simulation the Southern Hemisphere stratospheric jet is somewhat too strong.

Between April and July, the Northern Hemisphere tropospheric jet decreases in strength in the observations and to a greater extent in the control simulation, with the maximum zonal mean zonal wind for boreal summer being about 8 m s^{-1} too weak, as in the R21 simulation of McGregor et al. (1993, Fig. 9). The Southern Hemisphere simulation is again better, with the tropospheric jet only about 5 m s^{-1} too weak in July and the stratospheric jet close to observations.

During the second half of the year the Northern Hemisphere circulation increases in strength and the comparison between the observations and the control run improves. In October the Northern Hemisphere tropospheric jet cores for the observations and the control simulations are closely comparable in both their strengths and locations. The separation of the stratospheric jet in the Northern Hemisphere is evident in the observations in October but not in the control run. In fact the control run also underestimates the strength of the Northern Hemisphere stratospheric jet throughout the boreal winter season. In the Southern Hemisphere, the control simulation of the jet structure is quite good both in the troposphere and stratosphere, although the maximum strength of the tropospheric jet in October is about 5 m s^{-1} too weak compared with the observations. In November and December

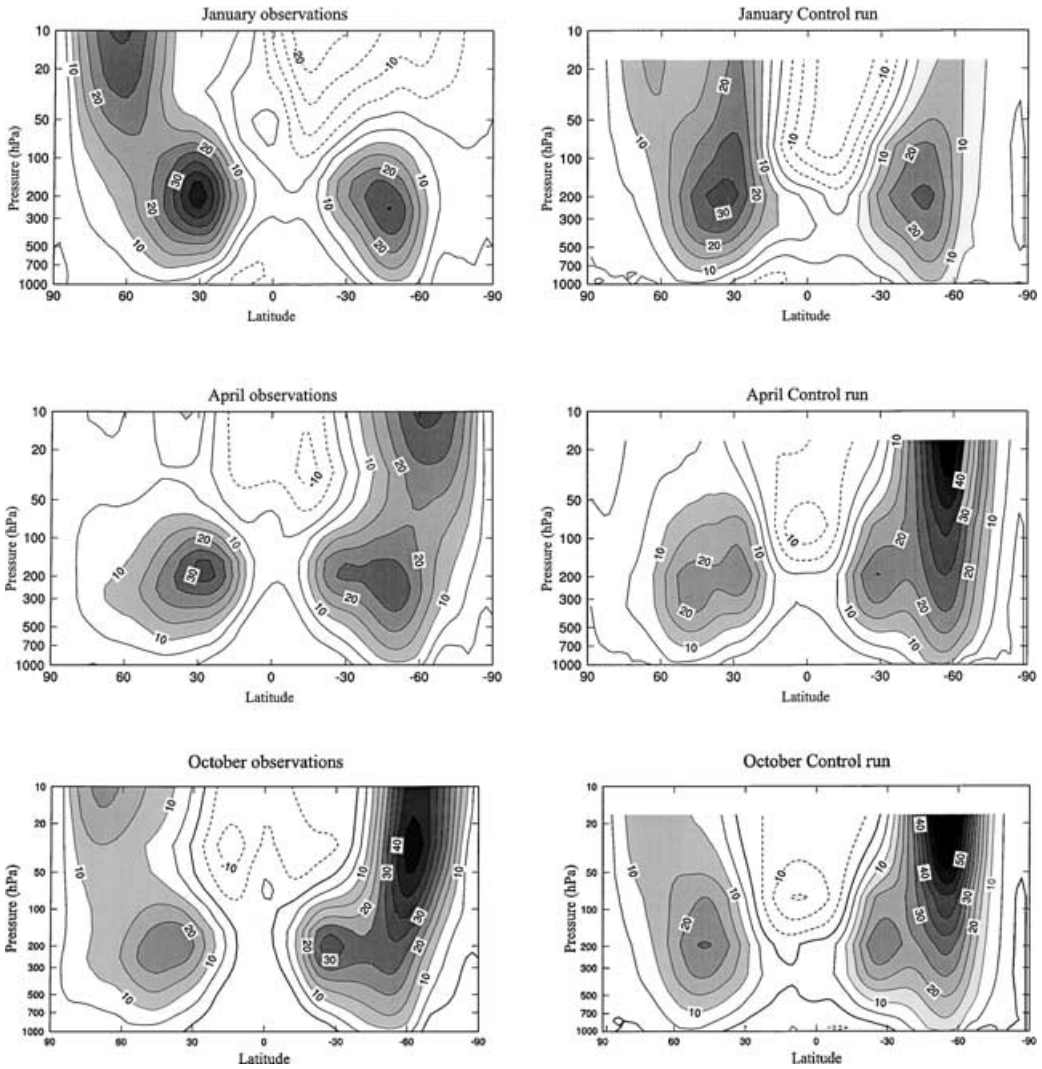

Fig. 4. Monthly and zonally averaged zonal wind cross-sections as functions of latitude and pressure based on ECMWF analyses for 1985 to 1992 and for control simulations.

(not shown), the Northern Hemisphere tropospheric circulation strengthens and the Southern Hemisphere circulation weakens in both the observations and the control run. As is the case for January however, the Northern Hemisphere tropospheric jet in the control has peak values which are underestimated by between 5 and 8 m s^{-1}.

In many respects the control simulations at T63 horizontal resolution are quite similar to the R21 simulations described by McGregor et al. (1993) and Watterson et al. (1995). This reflects the very similar physical parameterizations used in the two versions of the model. McGregor et al. (1993) give details of other circulation properties of the control simulations of the CSIRO model. These include zonal means of the meridional winds and temperatures, as functions of latitude and pressure, and latitude–longitude plots of sea-level pressure and 500 hPa zonal winds. The current T63 control simulations of these fields are broadly similar to the R21 results of McGregor et al. (1993) and will not be displayed here as our interest is primarily in the mean zonal winds (and kinetic energies).

4. GCM simulations with net eddy viscosity parameterization

4.1. Net eddy viscosity parameterization

In this section we parameterize the horizontal diffusion in terms of the normalized net dissipation function $g(n/n_*)$ of Fig. 1, where $n_* = 63$ for our T63 simulations; vertical diffusion is parameterized as described in Section 3. The tendency terms associated with the FD net eddy diffusion then take the forms

$$\frac{\partial \hat{\zeta}_{mn}}{\partial t} \sim -S[0.067\Omega]g(n/n_*)\hat{\zeta}_{mn} \sim -S\frac{\tilde{K}_\zeta^{\mathrm{d}}}{a^2}\left[g(n/n_*)n_*(n_*+1)\right]\hat{\zeta}_{mn} \tag{4.1a}$$

$$\frac{\partial \hat{D}_{mn}}{\partial t} \sim -S\frac{\tilde{K}_D^{\mathrm{d}}}{a^2}\left[g(n/n_*)n_*(n_*+1)\right]\hat{D}_{mn} \tag{4.1b}$$

$$\frac{\partial \hat{T}_{mn}}{\partial t} \sim -S\frac{\tilde{K}_T^{\mathrm{d}}}{a^2}\left[g(n/n_*)n_*(n_*+1)\right] \times\left\{\hat{T}_{mn} - \left(\bar{T} + \sigma\frac{\partial \bar{T}}{\partial \sigma} - T_{\mathrm{o}}\right)p_{\mathrm{s}mn}\right\} \tag{4.1c}$$

where [from Eq. (2.1)] $\tilde{K}_\zeta^{\mathrm{d}} = \frac{0.067a^2\Omega}{n_*(n_*+1)} = 4.92 \times 10^4$ $\mathrm{m^2\,s^{-1}}$ since $n_* = 63$. The dimensional vorticity diffusion coefficient $\tilde{K}_\zeta^{\mathrm{d}}$ corresponds to a nondimensional diffusion coefficient of $\tilde{K}_\zeta = 1.662 \times 10^{-5}$. The diffusion in Eq. (4.1) is slightly weaker than in the standard parameterization (Section 3) when $S = 1$, but larger in the runs using larger scaling coefficients. As in Section 3, we take $\tilde{K}_T^{\mathrm{d}} = \tilde{K}_\zeta^{\mathrm{d}}$ and $\tilde{K}_D^{\mathrm{d}} = 4\tilde{K}_\zeta^{\mathrm{d}}$. Apart from the scaling factor S, Eqs. (4.1a)–(4.1c) have the same form as Eqs. (3.1a)–(3.1c), respectively, but with the replacement

$$\Delta(n)n(n+1) \rightarrow g(n/n_*)n_*(n_*+1). \tag{4.2}$$

Note that both these functions have the value $n_*(n_*+1)$ at $n = n_*$.

The normalized net dissipation function $g(n/n_*)$ appears to be almost a universal function of n/n_* although the strength of the negative contribution in Fig. 1 may be reduced somewhat at higher resolution as noted in Section 2. Therefore, we have performed T63 GCM simulations with both $g(n/n_*)$ and $g^+(n/n_*)$, the positive part of g, viz.,

$$g^+(n/n_*) = \begin{cases} g(n/n_*) & \text{if } g \geq 0 \\ 0 & \text{otherwise.} \end{cases} \tag{4.3}$$

For barotropic flows near 500 hPa scaling factors of $S = 1$ and $S \approx 3$ would be appropriate at resolutions of T31 and T63, respectively (Section 2). At 200 or 300 hPa the results of Koshyk and Boer (1995) suggest that a scaling factor of $S \approx 5$ would be most appropriate at resolution T63. We shall in fact examine the sensitivity of the GCM results to the magnitude of the scaling factor, which is taken to be independent of height. We consider cases with $S = 1$, 5 and 10 and dissipation function g^+, denoted as runs *S*1, *S*5 and *S*10 respectively, and a case with $S = 5$ and dissipation function g, denoted as run *N*5. The results presented in the following subsections are based on 10 yr of model data to generate the monthly averages.

4.2. Kinetic energy spectra

Figure 5 shows the mean dimensional total wavenumber kinetic energy spectrum $e(n)$ in $\mathrm{m^2\,s^{-2}}$ for January for the *S*1, *S*5, *S*10 and *N*5 simulations, and the observed January 1979 spectrum is shown for comparison. The model results are based on averages over 10 Januaries. We see that the energy spectra for *S*5 and *S*10 follow the observed spectra quite well at most scales, with the main differences between *S*5 and *S*10 occurring at the very small scales. The *N*5 spectrum also closely follows the observed spectrum at wavenumbers smaller than about 25, but for larger

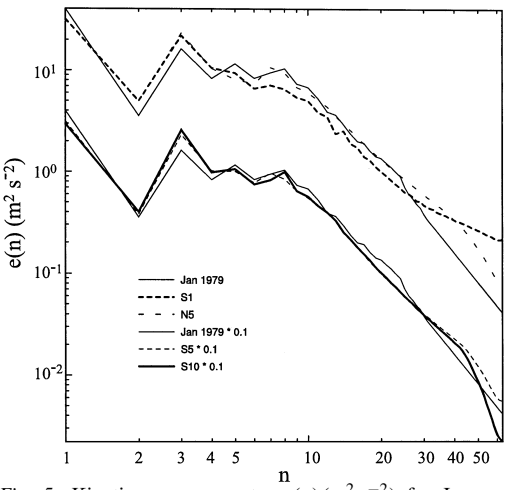

Fig. 5. Kinetic energy spectra $e(n)\,(\mathrm{m^2\,s^{-2}})$ for January 1979 (thin solid), *S*1 run (thick short dashed), *N*5 run (thin long dashed), *S*5 run ($\times 10^{-1}$) (thin short dashed) and *S*10 run ($\times 10^{-1}$) (thick solid) where the simulations are all for January.

wavenumbers there is some overestimation of the energy compared with the continued n^{-3} spectum.

With scaling factors of $S = 5$ or 10 the simulated kinetic energy spectra in Fig. 5 closely follow the observed January spectrum. The simulations using the height-independent FD net diffusion function appear to be no less skilful in replicating the observed kinetic energy spectrum than the simulations of Koshyk and Boer (1995) with height-dependent EIFs. Interestingly Kaas et al. (1999) found that their EIFs were more equivalent barotropic than those of Koshyk and Boer (1995) throughout most of the troposphere and were somewhat model-dependent. As expected on the basis of the arguments of Section 4.1, the *S*1 spectrum underestimates the kinetic energy at total wavenumbers between 5 and 25 and has too large an energy at the largest wavenumbers. In these respects it is similar to the control simulation's spectrum.

The results in Fig. 5 are further examples of the 'tail wagging the dog' effect. This effect is also evident in the different zonal wavenumber spectra $E(m)$ (not shown). For example, as the dissipation strength increases from the control to *S*5, *N*5 and *S*10 the zonal mean kinetic energy increases from $E(0) = 72.6$ to 75.7, 75.8 and 77.4 $m^2\ s^{-2}$, respectively. These increases are only moderate, but are nevertheless reflected in the mean zonal winds as discussed below.

Next we examine the seasonal dependence of energy spectra for the *S*10 simulation. Figure 6 shows the mean and mean $\pm$ standard deviation of the total wavenumber kinetic energy spectra $e(n)$ for January, April, July and October. These results were calculated on the basis of twice daily data for 10 yr for each month shown. The $E(m)$ spectra (not shown) closely follow an m^{-3} spectrum for $m \approx 8$–35 in each month, while the $e(n)$ spectra are slightly shallower than an n^{-3} spectrum for $n \approx 15$–35. The *S*10 run $e(n)$ spectra in fact appear to closely match the observed results of Straus and Ditlevsen (1999). We also note that the main seasonal changes in the spectra occur for the largest scales in the $e(n)$ spectra, with the shape and magnitudes at intermediate and small scales of the spectra showing much less change.

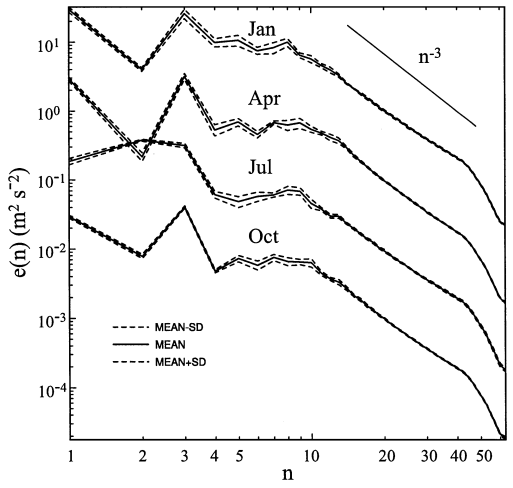

Fig. 6. Kinetic energy spectra $e(n)$ ($m^2\ s^{-2}$) (solid) and $e(n) \pm \sigma(n)$ (dashed) for *S*10 simulations for January, April ($\times 10^{-1}$), July ($\times 10^{-2}$) and October ($\times 10^{-3}$).

4.3. *Transient kinetic energy cross-sections*

The improved energy spectra for the *S*10 simulation (and for the *S*5 and *N*5 runs) shown in Figs. 5 and 6 are also reflected in better agreement between simulated and observed transient kinetic energy in physical space. Figure 7 shows cross sections of zonally averaged transient kinetic energy based on twice daily data for January for 10 yr of integration. We note the considerable improvements in the maximum transient kinetic energy in the Northern Hemisphere tropospheric jet core, which is now considerably closer to those of the observations (Fig. 3a) compared with the control run results (Fig. 3b). For example, in the Northern Hemisphere the peak transient kinetic energy in the *S*10 run is 215 $m^2\ s^{-2}$ compared with 189 $m^2\ s^{-2}$ for the control and 220 $m^2\ s^{-2}$ at 300 hPa near 50°N and 231 $m^2\ s^{-2}$ at 250 hPa near 40°N in the observations. In the Southern Hemisphere the peak transient kinetic energy in the *S*10 run is again improved compared with the control but is still significantly lower than in the observations;

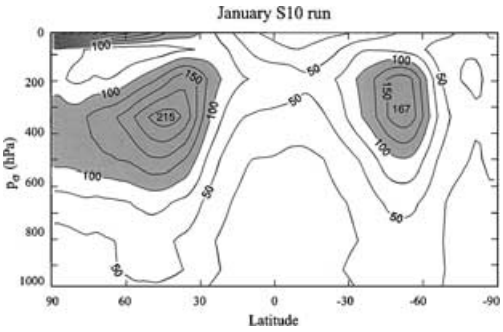

Fig. 7. As in Fig. 3b for the *S*10 simulation.

the peak values are 167, 144 and 219 $m^2\ s^{-2}$ for the *S*10, control and observations, respectively. The *S*10 simulation used a 15-min time-step and, unlike the control simulation with this time-step (discussed in Section 3), did not result in spurious transients over the southern polar latitudes.

The deficit in physical space transient kinetic energy in the control simulation for January (Fig. 3b) is reflected in Fig. 2 by too little kinetic energy between wavenumbers 5 and 12. In contrast, the kinetic energy spectra for the *S*10 and *S*5 and *N*5 runs closely follow the observed spectra at large and intermediate wavenumbers, giving the improved physical space transient kinetic energy (Fig. 7 for the *S*10 run).

4.4. Mean zonal winds

Next, we examine the mean circulations for the *S*5, *N*5 and *S*10 simulations. Figure 8 shows the mean zonal winds for January and April as functions of latitude and pressure for the *S*5 run. These results and others presented in this subsection are based on twice daily data taken from 10 yr of integrations. Also shown are the differences between the *S*5 results and the control simulation of Section 4. Differences that are statistically significant at the 95% confidence level according to Student's *t*-test are shaded. The *t*-test is based on 10 monthly averages for each month shown. In general, the differences are statistically significant where their magnitudes are larger than about 1 $m\ s^{-1}$. Figure 9 shows the corresponding mean zonal winds in January in the *N*5 simulations. There is a close similarity between the *S*5 and *N*5 results both in January and in other months (not shown), indicating that the

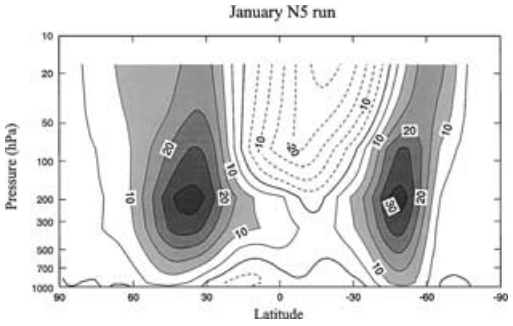

Fig. 9. As in Fig. 4 for the *N*5 simulation.

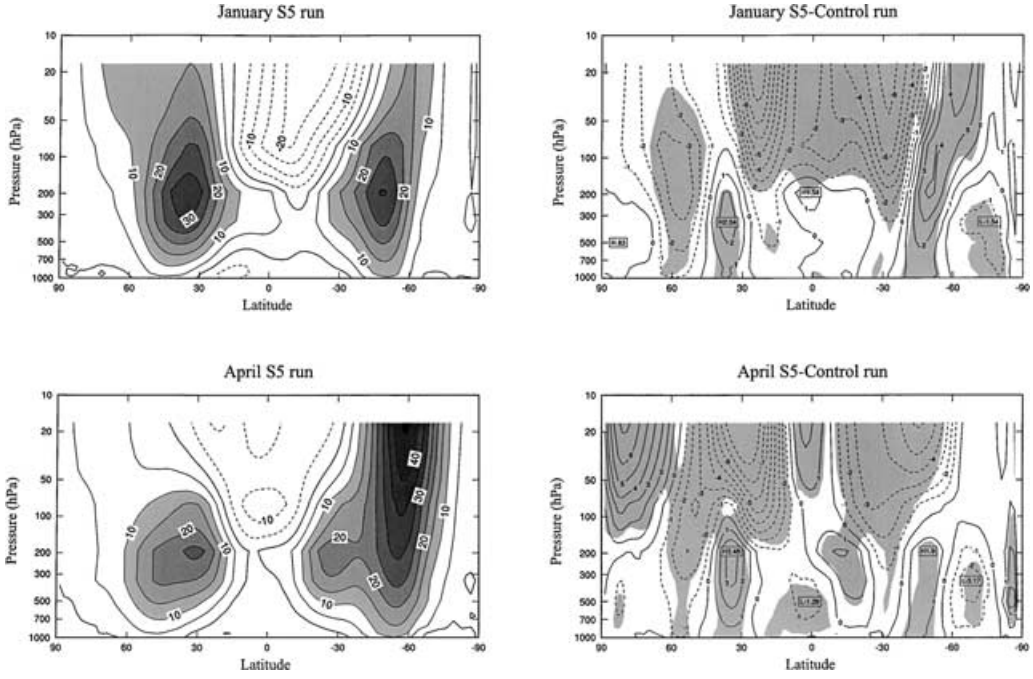

Fig. 8. As in Fig. 4 for the *S*5 simulation and differences between *S*5 and control simulations; on the difference plots results that are statistically significant at the 95% confidence level, according to the Student *t*-test, are shaded.

mean zonal winds are relatively insensitive to whether the dissipation function $g^+(n/n_*)$ or $g(n/n_*)$ is used. For January, tropospheric differences between the *N*5 and *S*5 runs are generally less than 2 m s^{-1}, with some local stratospheric differences reaching 3.5 m s^{-1}; the tropospheric jet between 200 and 300 hPa is 2 m s^{-1} weaker at 35°N and 2 m s^{-1} stronger at 45°S in the *N*5 run compared with the *S*5 run.

From Fig. 8 we see that in January the net dissipation in the *S*5 run strengthens the Northern Hemisphere tropospheric jet by about 2.5 m s^{-1} and moves it slightly equatorward compared with the control mean winds. The Southern Hemisphere tropospheric jet is also strengthened by about 4 m s^{-1}. In these respects the net eddy dissipation function g^+ improves the simulations over the control. The net dissipation also increases the strength of the easterly stratospheric flow in the tropical and subtropical latitudes; above 100 hPa the strength of the flow is largely determined by the strength of the gravity wave drag parameterization used, and it may be that increasing its strength would improve the overall simulation. It also seems likely that reducing the strength of the diffusion in the stratosphere would decrease the easterly winds in the tropics and subtropics. This would entail having the strength of the diffusion being height-dependent, and so would be at the expense of an empirical height-dependent function. We shall not experiment with such functions here but leave their determination for a subsequent study.

In April, the Northern Hemisphere tropospheric jet core for the *S*5 simulations increases in strength by about 3.5 m s^{-1} compared to the control, and there is better focussing of the jet maximum near 30° latitude. In these respects the *S*5 runs compare better with the observations. In the Southern Hemisphere the improvements in the tropospheric jet strength are less. For the other boreal winter and spring months the improvements in the mean tropospheric winds in the *S*5 runs are similar to those shown for January and April. During boreal summer (not shown), particularly in July, there is much less change in the tropospheric extratropics in the *S*5 runs. There is some reduction in the tropospheric easterlies but little change in the too weak Northern Hemisphere tropospheric jet. It is clear that there are significant deficiencies in the physical parameterizations that manifest themselves in the too weak Northern Hemisphere jet during boreal summer. The net eddy dissipation parameterization is not able to compensate for these deficiencies.

In boreal autumn (not shown) there are again increases in the zonal winds in the tropospheric jet cores in both the Northern Hemisphere and Southern Hemisphere in the *S*5 run compared with the control run. For example, in October the increase is about 2 m s^{-1} between 200 and 300 hPa at both 35°N and 45°S. By December (not shown) there are further increases in the peak values of zonal winds in the troposphere of 3.5 m s^{-1} in the Northern Hemisphere, at 300 hPa and 40°N, and 5.6 m s^{-1} in the Southern Hemisphere, at 200 hPa and 45°S, compared with the control run.

Figure 10 shows the same fields as in Fig. 8 but for the *S*10 simulations, i.e. the mean zonal winds for January and April and differences between the *S*10 and control runs. The qualitative differences between the *S*10 – control and *S*5 – control results are similar, but their magnitudes are generally larger in the *S*10 case involving the stronger diffusion. For example, in January and April the peak zonal winds in the Northern Hemisphere tropospheric jet core increase by nearly 5 m s^{-1} compared with the control, giving better comparisons with observations. The Southern Hemisphere jet core is also moved equatorward in the *S*10 simulation compared with the control and strengthened by nearly 5 m s^{-1} in boreal winter and nearly 3 m s^{-1} in boreal spring. Again in boreal summer (not shown) there is little change in the relatively weak Northern Hemisphere tropospheric jet in the *S*10 run compared with the control, indicating likely deficiencies in the physical parameterizations described above. There is again an increase in the tropospheric jet maximum in October of 2 m s^{-1} in the *S*10 run, and further increases occur in December of around 3 m s^{-1} in the Northern Hemisphere and Southern Hemisphere troposphere jet cores; the locations of these increases are as described for the *S*5 run.

5. Discussion and conclusions

We have examined the effects of implementing the net eddy viscosity of Frederiksen and Davies (1997; FD) as a horizontal diffusion parameterization within the CSIRO Mark 2 atmospheric GCM. The form of the FD net eddy viscosity was derived self-consistently from closure theory in such a way that it would maintain the same large-scale kinetic energy spectra, consistent with January 1979 observations, in the barotropic vorticity equation with changing resolution. We have examined the ability of the GCM to simulate

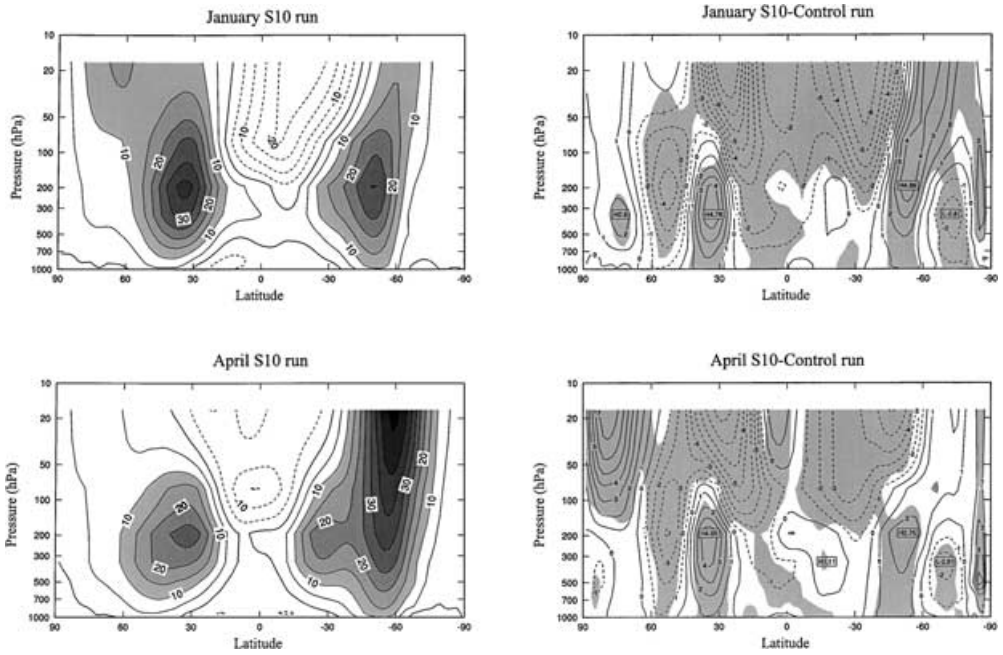

Fig. 10. As in Fig. 8 for the *S*10 simulation.

the annual cycle of zonal winds and transient kinetic energy with the FD diffusion parameterization. We have studied the sensitivity of our results to the strength of the diffusion measured by a height-independent scaling factor *S*. The latitude–pressure cross-sections of monthly and zonally averaged zonal winds and transient kinetic energy have been compared with observations and with control simulations using the standard diffusion parameterization employed in previous studies with this model (e.g. Smith et al., 1998; Smith, 1999 and references therein). We have also compared and contrasted zonal and total wavenumber spectra of kinetic energy for the FD parameterization with observations and with control simulations.

For scaling factors *S* between 5 and 10, the FD parameterization has improved the simulations of the CSIRO GCM in a number of ways. Throughout the annual cycle, both the zonal and total wavenumber spectra now have approximate -3 power laws for a range of intermediate wavenumbers, as in the observations (Wiin-Nielsen, 1967, 1972; Boer and Shepherd, 1983; Nastrom et al., 1984; Nastrom and Gage, 1985) and as expected theoretically (Kraichnan, 1967; 1971; Leith, 1971), while the control simulation spectra are flatter. In physical space, peak values of transient kinetic energy in the S10 run ($S = 10$) have increased considerably over the control results, giving better agreement with the observations. For example, in January monthly and zonally averaged transient kinetic energies are 26 m^2 s^{-2} larger near the Northern Hemisphere tropospheric jet core and 23 m^2 s^{-2} larger near the Southern Hemisphere tropospheric jet core in the *S*10 run compared with the control. The *S*10 model is stable with a larger 15-min time-step, while in the control large-amplitude spurious transients are generated throughout the atmosphere over the south polar latitudes if the time-step used exceeds 4 min. The strength of the dissipation in the *S*10 run and also its different form contribute to the stability.

The strength and location of the tropospheric jets are also improved with the FD parameterization in boreal autumn, winter and spring. For the *S*10 run, the monthly and zonally averaged zonal wind in the Northern Hemisphere and Southern Hemisphere tropospheric jet cores is stronger than in the control by as much as 5 m s^{-1} in boreal winter and spring. In the control simulations the tropospheric jet maxima tend to be located poleward of the observed jets, while for the *S*10 run this problem is largely rectified. In boreal summer, the Northern Hemisphere tropospheric jet is too weak in both the control and *S*10 simulations, indicating that there are deficiencies in the

thermodynamics of the model in this season for which the FD diffusion parameterization cannot compensate.

GCM simulations employing height-independent FD diffusion (with S between 5 and 10) appear to be no less skilful than the integrations of Koshyk and Boer (1995) with height-dependent empirical interaction function (EIFs), particularly in replicating observed vertically integrated kinetic energy spectra. Unlike the perfect model experiments of FD, here the eddy diffusion is interacting with many other parameterisations in the GCM, and improvements in the simulations, while beneficial, are of course not perfect. Kaas et al. (1999) have noted that improvements in GCM simulations with EIFs are both model- and resolution-dependent, generally giving better results at higher resolution. They suggest that further improvements may be achievable by allowing the diffusion functions to depend on zonal as well as total wavenumbers. More generally it may be necessary to also parameterize the effects of the nondiagonal elements of the covariance matrix of eddy fluxes. Frederiksen (1999) has examined the dynamical subgrid scale parameterization problem for general barotropic flows over topography. From his expressions one would expect that the eddy-topographic force, which arises from the nondiagonal elements of the eddy flux covariance matrix and measures the interaction of subgrid scale eddies with retained scale topography, would play a significant role in determining the mean large-scale flow.

Indeed, there are aspects of our results and those of Koshyk and Boer (1995) and Kaas et al. (1999) which suggest that a parameterization of the eddy-topographic force may be a missing ingredient needed to further improve the simulations. Firstly, Kaas et al. (1999, Fig. 1) find significant differences in mean sea level pressure near the Antarctic orography between perpetual January simulations at T106 and T30 resolution, even though T30 orography is used in both simulations. These differences are only partly reduced and only in some of their simulations employing their EIF parameterizations. The situation here appears to be analogous to that for model ocean circulations (Holloway, 1992; Alvarez et al., 1994) where a parameterization of the eddy-topographic force is needed to generate realistic boundary currents near the bottom topography. Secondly, simulations incorporating the EIF parameterisations of Koshyk and Boer (1995, Fig. 10) and Kaas et al. (1999, Fig. 9) yield spectra with excessive values of kinetic energy at large wavenumbers. And our present GCM simulations also result in more realistic kinetic energy spectra at large wavenumbers with larger scaling factors S than one might theoretically expect. It may be that in the absence of an eddy-topographic force parameterization the eddy diffusion has the job of attempting to maintain the large-scale mean flow, as well as the large-scale transient flow, through the 'tail wagging the dog' effect, and therefore needs to be stronger than for purely nontopographic turbulence (FD).

It may be some time before atmospheric GCMs routinely incorporate parameterisations representing the nondiagonal elements of the covariance matrix of eddy fluxes, such as the eddy-topographic force. In the meantime, net eddy diffusion parameterizations representing the dynamical effects of subgrid scale eddies, such as presented by Koshyk and Boer (1995), FD, Kaas et al. (1999) and in the current study, may be profitably used to improve aspects of GCM simulations.

6. Acknowledgements

We thank Hal Gordon, John McGregor and Leon Rotstayn for helpful discussions on the structure and specifications of the CSIRO Mark 2 atmospheric GCM.

REFERENCES

Alvarez, A., Tintore, J., Holloway, G., Eby, M. and Beckers, J. M. 1994. Effect of topographic stress on the circulation in the western Mediterranean. *J. Geophys. Res*. **99**, 16053–16064.

Baer, F. and Alyea, F. N. 1971. Effects of spectral truncation on general circulation and long-range prediction. *J. Atmos. Sci*. **28**, 457–480.

Blackadar, A. K. 1962. The vertical distribution of wind and turbulent exchange in a neutral atmosphere. *J. Geophys. Res*. **67**, 3095–3102.

Boer, G. J. and Shepherd, T. G. 1983. Large-scale two-dimensional turbulence in the atmosphere. *J. Atmos. Sci*. **40**, 164–184.

Bottomley, M., Folland, C. K., Hsiung, J., Newell, R. E. and Parker, D. E. 1990. *Global ocean surface temperature atlas*. UK Met. Office, 20 pp. & 313 plates.

Dix, M. R. and Hunt, B. G. 1995. Chaotic influences and the problem of deterministic seasonal predictions. *Int. J. Climatol*. **15**, 729–752.

ECMWF, 1994. *The description of the ECMWF/WCRP level III — A global atmospheric data archive*. European Centre for medium-Range Weather Forecasts report, p. 22.

Eliasen, E. and Laursen, L. 1990. On the effects of horizontal resolution and diffusion in a two-layer general circulation model with a zonally symmetric forcing. *Tellus* **42A**, 520–530.

Frederiksen, J. S. 1999. Subgrid-scale parameterisations of eddy-topographic force, eddy viscosity and stochastic backscatter for flow over topography. *J. Atmos. Sci*. **56**, 1481–1494.

Frederiksen, J. S. and Davies, A. G. 1997. Eddy viscosity and stochastic backscatter parameterizations on the sphere for atmospheric circulation models. *J. Atmos. Sci*. **54**, 2475–2492.

Frederiksen, J. S. and Sawford, B. L. 1980. Statistical dynamics of two-dimensional inviscid flow on a sphere. *J. Atmos. Sci*. **37**, 717–732.

Frederiksen, J. S., Dix, M. R. and Kepert, S. M. 1996. Systematic energy errors and the tendency toward canonical equilibrium in atmospheric circulation models. *J. Atmos. Sci*. **53**, 887–904.

Gordon, H. B. and O'Farrell, S. P. 1997. Transient climate change in the CSIRO coupled model with dynamical sea-ice. *Mon. Weather Rev*. **125**, 875–907.

Hollingsworth, A., Cubasch, U., Tibaldi, S., Brankovic, C., Palmer, T. N. and Campbell, L. 1987. Mid-latitude atmospheric prediction on time scales of 10–30 days. In: *Atmospheric and oceanic variability* (ed. H. Cattle). Royal Meteorological Society, 117–151.

Holloway, G. 1992. Representing topographic stress for large-scale ocean models. *J. Phys. Oceanogr*. **22**, 1033–1046.

Kaas, E., Guldberg, A., May, W. and Déqué, M. 1999. Using tendency errors to tune the parameterization of unresolved dynamical scale interactions in atmospheric general circulation models. *Tellus* **51A**, 612–629.

Koshyk, J. N. and Boer, G. J. 1995. Parameterization of dynamical subgrid-scale processes in a spectral GCM. *J. Atmos. Sci*. **52**, 965–976.

Kraichnan, R. H. 1967. Inertial ranges in two-dimensional turbulence. *Phys. Fluids* **10**, 1417–1423.

Kraichnan, R. H. 1971. Inertial-range transfer in two- and three-dimensional turbulence. *J. Fluid Mech*. **47**, 525–535.

Laursen, L. and Eliasen, E. 1989. On the effects of the damping mechanisms in an atmospheric circulation model. *Tellus* **41A**, 385–400.

Leith, C. E. 1971. Atmospheric predictability and two-dimensional turbulence. *J. Atmos. Sci*. **28**, 145–161.

Leith, C. E. 1990. Stochastic backscatter in a subgrid-scale model. Plane shear mixing layer. *Phys. Fluids A* **2**, 297–299.

Manabe, S., Smagorinsky, J. and Strickler, R. F. 1965. Simulated climatology of a general circulation model with a hydrological cycle. *Mon. Wea. Rev*. **93**, 769–798.

Manabe, S., Smagorinsky, J., Holloway, J. L. and Stone, H. M. 1970. Simulated climatology of a general circulation model with a hydrologic cycle. Part III: Effects of increased horizontal computational resolutions. *Mon. Wea. Rev*. **98**, 175–212.

Manabe, S., Hahn, D. G. and Holloway, J. L. Jr. 1979. *Climate simulations with GFDL spectral models of the atmosphere: effect of spectral truncation*. GARP Pub. Ser. **22**, 41–94.

McGregor, J. L. 1993. Economical determination of departure points for semi-Lagrangian models. *Mon. Wea. Rev*. **121**, 221–230.

McGregor, J. L., Gordon, H. B., Watterson, I. G., Dix, M. R. and Rotstayn, L. D. 1993. *The CSIRO 9-level atmospheric general circulation model*. Melbourne, CSIRO Division of Atmospheric Research. (Technical Paper 26.)

Miyakoda, K., Strickler, R. F., Nappo, C. J., Baker, P. L. and Hembree, G. D. 1971. The effect of horizontal grid resolution in an atmospheric circulation model. *J. Atmos. Sci*. **28**, 481–499.

Nastrom, G. D. and Gage, K. S. 1985. A climatology of atmospheric wavenumber spectra observed by commercial aircraft. *J. Atmos. Sci*. **42**, 950–960.

Nastrom, G. D., Gage, K. S. and Jasperson, W. H. 1984. The atmospheric kinetic energy spectrum, 10°–10^4 km. *Nature* **310**, 36–38.

Piomelli, U., Cabot, W. H., Moin, P. and Lee, S. 1991. Subgrid-scale backscatter in turbulent and transitional flows. *Phys. Fluids A* **3**, 1766–1771.

Smagorinsky, J., Manabe, S. and Holloway, J. L. 1965. Numerical results from a nine-level general circulation model of the atmosphere. *Mon. Wea. Rev*. **93**, 727–768.

Smith, I. N. 1999. Estimating mass balance components of the Greenland ice sheet from a long-term GCM simulation. *Global and Planetary Change* **20**, 19–32.

Smith, I. N., Dix, M. and Allan, R. J. 1997. The effect of greenhouse SSTs on ENSO simulations with an AGCM. *J. Climate* **10**, 342–352.

Smith, I. N., Budd, W. F. and Reid, P. 1998. Model estimates of Antarctic accumulation rates and their relationship to temperature and changes. *Ann. Glaciol.* **27**, 246–250.

Straus, D. M. and Ditlevsen, P. 1999. Two-dimensional turbulence properties of ECMWF reanalyses. *Tellus* **51A**, 749–772.

Watterson, I. G., Dix, M. R., Gordon, H. B. and McGregor, J. L. 1995. The CSIRO nine-level atmospheric general circulation model and its equilibrium and doubled CO_2 climates. *Aust. Meteorol Mag*. **44**, 111–125.

Watterson, I. G., O'Farrell, S. P. and Dix, M. R. 1997. Energy and water transport in climates simulated by a general circulation model that includes dynamic sea ice. *J. Geophys. Res*. **102**, 11,027–11,037.

Wün-Nielsen, A. 1967. On the annual variation and spectral distribution of atmospheric energy. *Tellus* **19**, 540–559.

Wün-Nielsen, A. 1972. A study of power laws in the atmospheric kinetic energy spectrum using spherical harmonic functions. *Meteor. Ann*. **6**, 107–124.